Spiral Phyllotaxis: The Natural Way to Construct a 3D Radial Trajectory in MRI

Davide Piccini,[1*] Arne Littmann,[2] Sonia Nielles-Vallespin,[2] and Michael O. Zenge[2]

While radial 3D acquisition has been discussed in cardiac MRI for its excellent results with radial undersampling, the self-navigating properties of the trajectory need yet to be exploited. Hence, the radial trajectory has to be interleaved such that the first readout of every interleave starts at the top of the sphere, which represents the shell covering all readouts. If this is done sub-optimally, the image quality might be degraded by eddy current effects, and advanced density compensation is needed. In this work, an innovative 3D radial trajectory based on a natural spiral phyllotaxis pattern is introduced, which features optimized interleaving properties: (1) overall uniform readout distribution is preserved, which facilitates simple density compensation, and (2) if the number of interleaves is a Fibonacci number, the interleaves self-arrange such that eddy current effects are significantly reduced. These features were theoretically assessed in comparison with two variants of an interleaved Archimedean spiral pattern. Furthermore, the novel pattern was compared with one of the Archimedean spiral patterns, with identical density compensation, in phantom experiments. Navigator-gated whole-heart coronary imaging was performed in six healthy volunteers. High reduction of eddy current artifacts and overall improvement in image quality were achieved with the novel trajectory. Magn Reson Med 66:1049–1056, 2011. © 2011 Wiley-Liss, Inc.

Key words: radial 3D; coronary MRI; spiral phyllotaxis; eddy currents

INTRODUCTION

In botany, phyllotaxis is the arrangement of leaves on a stem. The pattern known as "spiral phyllotaxis" is an eye-catching arrangement, consisting of two sets of spirals forming a lattice. This pattern can be identified in a great number of plants and flowers, where the visible spirals going clockwise and counter-clockwise are typically associated with two successive elements of the Fibonacci sequence. In these cases, the angle between successive leaves is always close to the golden angle. Extensive studies on spiral phyllotaxis and its mathematical properties have been reported in many scientific fields within natural sciences (1), theoretical sciences (2–5), and also engineering applications (6). The use of sampling strategies and reconstruction techniques involving Fibonacci numbers (7) and the golden angle (8–10) is also known in MRI. These methods feature properties that are particularly well suited for cardiac MRI applications.

In the field of cardiac MRI, it has to be considered that the anatomy of the heart is very complex. Furthermore, in many cases, the location and orientation of the heart differ individually within the thorax. Up to now, only experienced operators are able to perform a comprehensive cardiac MR examination. As a consequence, the option to acquire a 3D volume that covers the whole heart with high and isotropic resolution is a much desirable goal (11). In this configuration, some of the preparatory steps of a cardiac examination are obsolete since the complexity of slice planning is reduced significantly (12). In addition, it is possible to reconstruct views with arbitrary orientations off-line, e.g., curved reformats along the coronary vessels.

In this context, 3D radial sampling offers two pronounced general advantages compared with Cartesian sampling. The method is: (1) less sensitive to radial undersampling (13–15), which manifests streaking artifacts, smearing and increased pseudo-noise, rather than discrete aliasing artifacts and (2) intrinsically robust with respect to motion artifacts (16), for displacements oriented perpendicularly to the readout direction are not resolved. Besides these advantages, image reconstruction methods for radial MRI involve sampling density compensation (17,18). The complexity of the density compensation algorithm can be reduced if the radial readouts are distributed uniformly.

Cardiac imaging is performed in the presence of periodic contraction of the imaged object as well as respiratory motion. While the contraction of the heart is frozen in a specific data acquisition window of the cardiac cycle by electrocardiogram triggering (ECG triggering) (19), respiratory artifacts are reduced with the use of respiratory gating (20,21). This results in a highly interleaved data acquisition scheme. In the case of 3D radial MRI, information about the respiratory motion of the heart can be extracted directly from the readouts that are oriented along the superior-inferior (SI) direction (22). In this scenario, rapidly changing gradient moments have to be carefully avoided to prevent eddy current effects when a balanced Steady-State Free Precession (SSFP) sequence is used for acquisition. Signal oscillations in a balanced gradient scheme, in fact, result in image artifacts, as recently reported, for Cartesian sampling, in (23). Thus, a 3D radial trajectory that is optimally suited for cardiac MRI features: (1) uniform distribution of the readouts and (2) interleaving properties that minimize eddy current effects.

In the present work, an innovative 3D radial trajectory based on a spiral phyllotaxis pattern is introduced, which integrates both an overall uniform distribution of the readouts and optimized interleaving properties. This trajectory is, furthermore, intrinsically prepared for self-navigated cardiac MRI. These features of the new approach were

[1]Department of Computer Science, Pattern Recognition Lab, Friedrich-Alexander University of Erlangen-Nuremberg, Erlangen, Germany
[2]MR Applications and Workflow Development, Healthcare Sector, Siemens AG, Erlangen, Germany

*Correspondence to: Davide Piccini M.Sc., Pattern Recognition Lab, Department of Computer Science, Friedrich-Alexander University of Erlangen-Nuremberg, Martensstr. 3, D-91058 Erlangen, Germany. E-mail: davide.piccini@informatik.uni-erlangen.de

Received 8 July 2010; revised 30 January 2011; accepted 7 February 2011.
DOI 10.1002/mrm.22898
Published online 5 April 2011 in Wiley Online Library (wileyonlinelibrary.com).

theoretically assessed in comparison with two alternative 3D radial trajectories based on two different implementations of an Archimedean spiral pattern. In addition, the image quality achieved with the novel trajectory in phantoms was compared with that of images acquired with one alternative trajectory. Both were reconstructed with identical density compensation. Finally, the experiments were repeated for navigator gated whole-heart coronary MRI in six healthy volunteers.

THEORY

In a straightforward approach, a 3D radial trajectory can be implemented with an Archimedean spiral pattern (24,25). In this case, the revolutions of the origins of the linear readouts on a sphere in k-space get both tighter and more densely sampled in proportion to the total number of readouts, N. This approach provides a simple formulation for a 3D radial trajectory and allows for a uniform distribution of the readouts.

Spiral Phyllotaxis Pattern

In the year 1979, the German physicist H. Vogel published a closed formula for the spiral phyllotaxis pattern in 2D (3). To provide a dense and uniform sampling for 2D fast cardiac MRI sequences, a solution featuring Vogel's formula had already been proposed in (7) but limited to the frequency-encoding plane. In the current work, the formulation in 2D polar coordinates of the original pattern was extended to 3D spherical coordinates (26):

$$r = \text{const.}, \quad [1]$$

$$\varphi_n = \frac{(2\pi)}{360} \cdot n \cdot \varphi_{\text{gold}}, \quad [2]$$

$$\theta_n = \frac{\pi}{2} \cdot \sqrt{\frac{n}{N}}. \quad [3]$$

While the radius, r, is constant, the azimuthal angle, φ_n, of a readout $n = 1, 2, \ldots N$ going through the center of k-space is proportional to the golden angle, $\varphi_{\text{gold}} = 137.51°$. Polar angles, θ_n, are calculated in proportion to the square root of n over the total number of readouts, N, that are used to sample the whole 3D space. An example of the overall distribution of the readouts on the half sphere is displayed in Fig. 1 both in a top view and angulated view.

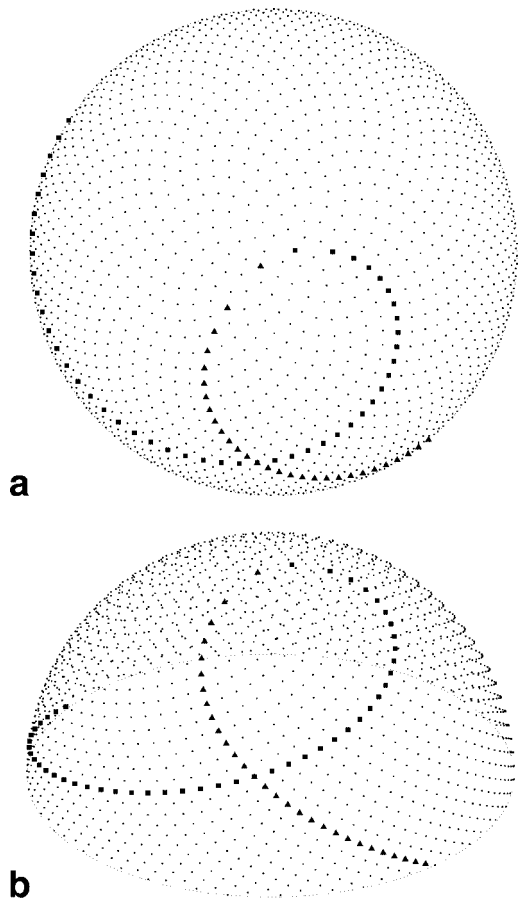

FIG. 1. Distribution of the origins of the readouts in a 3D spiral phyllotaxis pattern with $N = 1600$ radial readouts in top view (**a**) and angulated view (**b**). Each dot represents the origin of a linear readout going through the center of k-space. The elements of two eye-catching spirals running clockwise (squares) and counterclockwise (triangles) are highlighted in the plot. These spirals are associated with interleaving the trajectory with 34 and 55 interleaves, respectively, which are two successive Fibonacci numbers.

Interleaving

Since cardiac MRI data acquisition is performed in a highly interleaved fashion, the 3D radial trajectory needs to be adequately prepared. Thus, a total number of readouts $N = M \cdot P$ can be straightforwardly interleaved in M interleaves with P readouts per interleave just by assigning every Mth readout to a specific interleave. This results in an overall uniform distribution of the total number of readouts on the sphere. An alternative approach, in the context of 3D radial MRI, was recently proposed in (16) to avoid eddy current effects with self-gated cardiac MRI. In that solution, at first the pattern of a single interleave is constructed, e.g., an Archimedean spiral with P readouts. Then the single interleave is rotated M-times with a constant azimuthal angle. Although this leads to an increased density of readouts originating from the top of the sphere, the displacement of successive readouts within one interleave is significantly reduced. Henceforth, the spiral Archimedean pattern interleaved with the straightforward method will be referred as type A, while the pattern interleaved with the rotation-based method will be referred as type B. In addition, when referring to the interleaved spiral phyllotaxis pattern, the straightforward interleaving method is always to be intended. In this sense, in Fig. 2, columns (a) and (b) illustrate the differences between the type A approach and the type B approach, respectively. In comparison, the interleaving properties of the spiral phyllotaxis pattern, are plotted in columns (c) and (d). While in case of an Archimedean spiral pattern, the uniform distribution of the readouts excludes small displacements of successive readouts, the interleaved spiral phyllotaxis pattern integrates both features. If the number of interleaves is a Fibonacci number (Fig. 2, column (d)), then

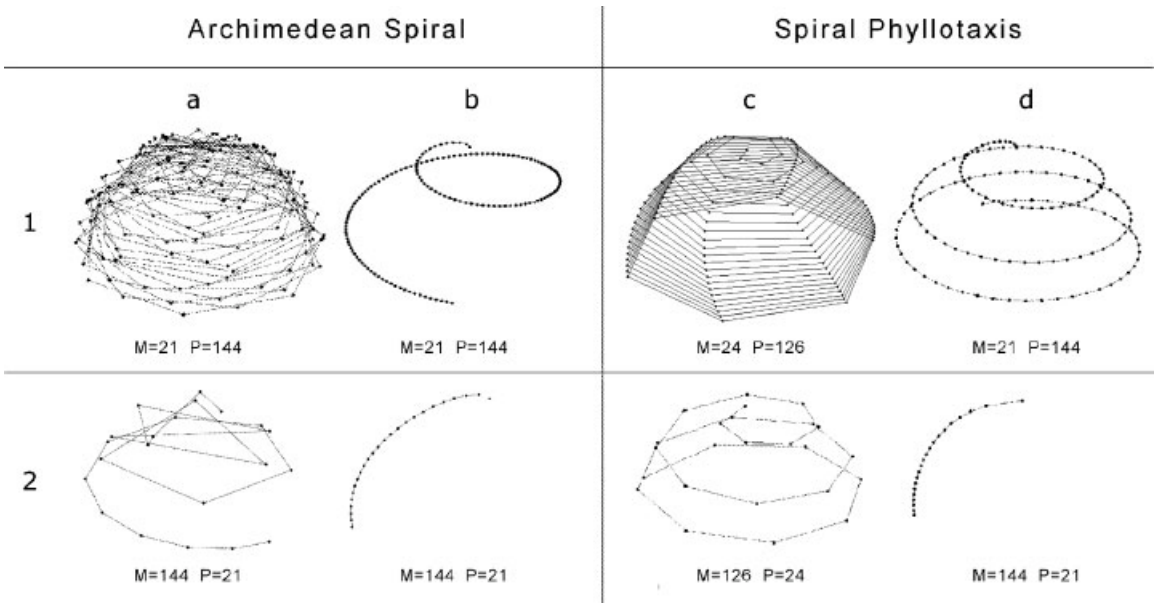

FIG. 2. Visualization of the differences of the interleaving techniques of the uniform Archimedean spiral pattern in the columns (**a**) and the nonuniform Archimedean spiral pattern (**b**) in comparison with the properties of the spiral phyllotaxis pattern, when interleaved in the straightforward way, in the columns (**c**) and (**d**). Each plot represents one of M interleaves with P readouts out of a total number of $N = M \cdot P = 3024$. In row (1) M is much smaller than P, whereas row (2) represents the highly interleaved case with M larger than P. Dots represent the origins of linear readouts which run through the center of k-space. Straight lines connecting successive readouts represent the change of the gradient moment from one readout to the next. In the case of the Archimedean spiral patterns, either an overall uniform distribution of the readouts is achieved with the straightforward interleaving approach (type A) of (a.1) and (a.2) or the displacement of successive readouts is minimized with the rotation-based approach (type B) of (b.1) and (b.2). Unless the number of interleaves is a non-Fibonacci number (c.1), (c.2) the spiral phyllotaxis pattern, straightforwardly interleaved, integrates both features (d.1), (d.2). In this latter case, the trajectory self-arranges in such a way that the displacements between successive readouts within one interleave are minimized and the rotation angle between successive interleaves equals the golden angle.

the trajectory self-arranges in such a way that the displacements between successive readouts within one interleave are minimized (2). Intrinsically, the actual rotation angle between successive interleaves is the golden angle.

MATERIALS AND METHODS

Theoretical Evaluation

The novel 3D spiral phyllotaxis pattern was compared with both the Archimedean spiral patterns of type A and type B, using simulations and analyses performed in Matlab 7.3 (The MathWorks Inc., Natick, MA). First, the general uniformity of the distribution of readouts was evaluated. For this purpose, the relative standard deviation (RSD) of the distances $d_{i,j}$ between each origin point i and each of its four closest neighbors j was calculated for all trajectories:

$$\mathrm{RSD} = \frac{\sqrt{\frac{1}{N\cdot 4}\cdot \sum_{i=1,j=1}^{i=N,j=4}(d_{j,i}-\mu_\mathrm{d})^2}}{\mu_\mathrm{d}}\cdot 100, \qquad [4]$$

with μ_d being the mean distance, defined as:

$$\mu_\mathrm{d} = \frac{1}{N\cdot 4}\cdot \sum_{i=1,j=1}^{i=N,j=4} d_{j,i}. \qquad [5]$$

The RSD was calculated for a constant number of readouts $P = 34$ per interleave, while the number of interleaves was increased following the Fibonacci series, with $M = [1, 2, 3, 5 \ldots 233, 377]$.

The aim of a second analysis was to provide a measure of the expected eddy current effects associated with each trajectory. Thus, the average distance of successive readouts within one interleave was calculated. This measure was done for each trajectory with a constant number of readouts $P = 34$ per interleave for an increasing number of interleaves $M = [1, 2, 3, 5 \ldots 233, 377]$.

Finally, the point spread function (PSF) of the radial 3D trajectory based on the Archimedean spiral pattern noninterleaved and that of the trajectory based on the radial 3D spiral phyllotaxis pattern were compared. Therefore, input data with 22% radial undersampling and $N = 12,818$ of both trajectories were initialized with constant values and were reconstructed using the same density compensation. The signal distribution of the two PSFs was visually analysed in three dimensions. Furthermore, the signal intensity of the central peaks and the mean signal intensities in two regions of interest comprising 400 pixels were compared in the central slice of a total number of 384 transversal slices with a 384 pixels squared matrix corresponding to a $2 \cdot \mathrm{FOV}$ (Field of View) representation.

MR Experiments

The presented 3D radial trajectory based on the spiral phyllotaxis pattern was implemented on a 1.5 T MAGNETOM

Avanto scanner (Siemens AG, Healthcare Sector, Erlangen, Germany) with software version B15A and was compared with an established implementation of the Archimedean spiral pattern (25) in phantoms and in vivo. Radial 3D data acquisition was performed with: (1) the uniform Archimedean spiral pattern, non interleaved, as the reference data, (2) the interleaved Archimedean spiral pattern of type A, and (3) the new 3D spiral phyllotaxis interleaved pattern. In all experiments, nonselective, T2-prepared, fat-saturated, balanced SSFP imaging was performed with the following parameters: TR/TE 3.0/1.52 ms, FOV $(220\,\text{mm})^3$, matrix 192^3, measured voxel size $(1.15\,\text{mm})^3$, flip angle 90°, and receiver bandwidth 898 Hz/Px. A total of 12,818 radial readouts were acquired in 377 interleaves for an overall undersampling ratio of 22%. Two-fold oversampling was applied in the readout direction. Image reconstruction was performed online with a gridding algorithm (17) featuring identical density compensation settings (27) for all protocols.

Experiments on a multi-purpose phantom were performed only with the body coil. Artifacts produced by eddy current effects in the interleaved Archimedean spiral and the interleaved spiral phyllotaxis were evaluated by qualitative comparison with the reference image data. Whole-heart coronary imaging was performed in six healthy volunteers after informed consent. A total of 12 elements of a body matrix coil (anterior) and the spine matrix coil (posterior) were selected for the acquisitions. The reference trajectory was acquired in a segmented fashion. The measurements were ECG-triggered and a subject-dependent delay was applied to position the data acquisition window in late diastole, where cardiac motion is expected to be minimal (19). To avoid artifacts caused by respiratory motion, gating was performed with a crossed-slice spin echo navigator placed on the dome of the right hemidiaphragm. In this case, the tolerance window was 5 mm. To extract the right coronary artery (RCA), the isotropic image data were reformatted during postprocessing with the curved cut tool in *syngo* 3D (Siemens AG, Healthcare Sector, Erlangen, Germany). The in vivo images were quantitatively evaluated for SNR, CNR and vessel sharpness of the RCA, as described in (28). For SNR and CNR, the mean blood signal intensities were measured in a cross-sectional plane of the ascending aorta at the RCA origin, while myocardial mean signal intensities were taken at the anterior portion of the left ventricular wall, inferior to the left anterior descending artery. Regions of interest for the measurement of noise were carefully placed in sections of the lungs with minimal streaking artifacts. Although it was not possible to generally avoid residual contribution of artifact noise, SNR and CNR were nevertheless considered a general image quality measure. The inverse of the average distance between the 20% and the 80% of the signal intensity profiles on both sides of a user-selected line perpendicular to the axes of the RCA was used for the calculation of the vessel sharpness.

RESULTS

The plot of the RSDs of the alternative implementations of the interleaved Archimedean spiral pattern in Fig. 3 confirms that for more than $M = 34$ interleaves the uniformity of the distribution of readouts of the type A pattern is very high with an RSD of less than 2%, whereas the uniformity of the type B pattern decreases with an increasing number of interleaves. Even with $M = 34$ interleaves the RSD is already >7%. In contrast to this, the RSD of the spiral phyllotaxis pattern is 6%–7% regardless of the number of

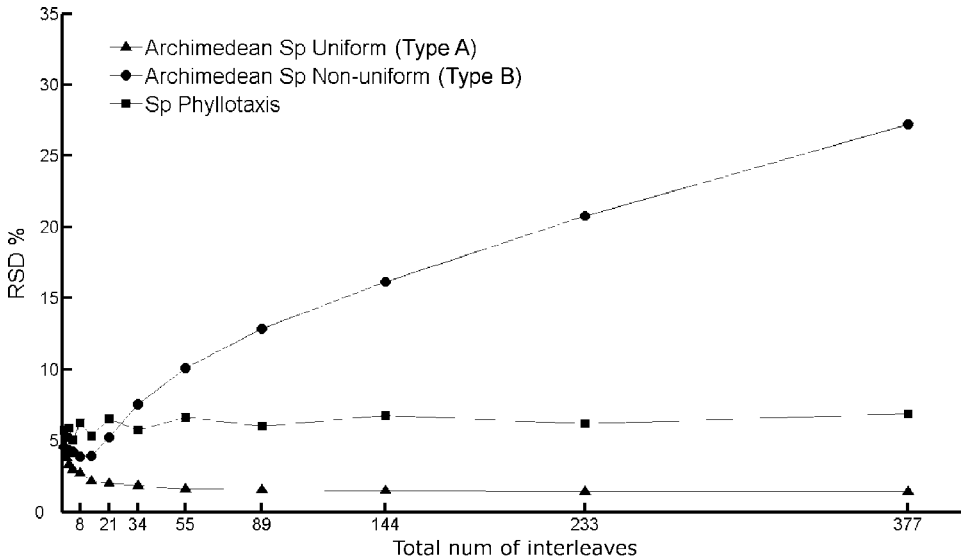

FIG. 3. Plots of the RSD of the distance between adjacent readouts on the sphere over the total number of interleaves. The distributions were simulated with a constant number of readouts per interleave ($P = 34$) for the three described methods. Increasing the total number of interleaves, the RSD of the uniform Archimedean spiral pattern decreases rapidly and remains very low, whereas the Archimedean spiral pattern implementing the nonuniform interleaving approach increases to significantly high values. The RSD of the spiral phyllotaxis pattern remains consistently low regardless of the number of interleaves. Even if the RSD of the spiral phyllotaxis is higher than the uniform Archimedean spiral, a density compensation algorithm for uniform distribution is considered to be sufficient.

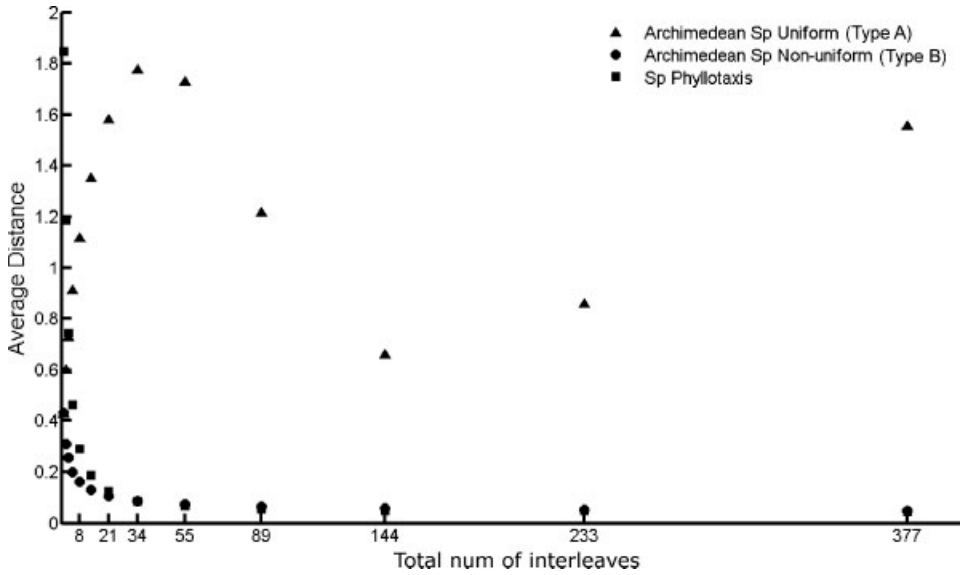

FIG. 4. Plots of the average distance between the origins of subsequent readouts within one interleave over the displayed total number of interleaves, computed only for Fibonacci numbers, for the three methods described. The mean distance is very high for the uniform Archimedean spiral pattern and shows no correlation with the number of interleaves. Both the spiral phyllotaxis and the nonuniform Archimedean spiral, on the other hand, show smooth gradient displacements and a similar decrease with the increase of the total number of interleaves, thus implying robustness to eddy current effects.

interleaves. For the average distance of successive readouts in one interleave, the performance of the two Archimedean spiral patterns is reversed, Fig. 4. For the type A compared with the type B pattern, the average distance of successive readouts is increased by about one order of magnitude. Furthermore, the average distance is uncorrelated with the number of interleaves. However, the mean distance of successive readouts of the spiral phyllotaxis pattern rapidly decreases with an increasing Fibonacci number of interleaves and is practically identical to the Archimedean spiral pattern of type B. The innermost parts of the two PSFs do not show any significant difference and, in general, each PSF individually features a very similar signal distribution in all planes containing the SI axis. However, the spatial distribution of the signal intensities in the evaluated volume displays prominent differences (Fig. 5). In the PSF of the Archimedean spiral pattern, in (a) and (c), a spherical volume around the center of k-space with very little streaking components can be identified. Although the transversal diameter of the corresponding central volume is smaller in the PSF of the spiral phyllotaxis pattern (d), the volume with minimal streaking is extended to a cylinder oriented along the SI direction (b). The signal intensity of the central peak of the PSFs is identically 4014 for both trajectories, the one based on the Archimedean spiral pattern and the other one based on the spiral phyllotaxis pattern. In the framed region labelled with number (1), the mean signal intensity is lower for the Archimedean spiral pattern, 0.16 ± 0.11, compared with the spiral phyllotaxis pattern, 0.25 ± 0.18. Nevertheless, the signal intensity of the framed region (2) in the PSF of the novel trajectory, 0.48 ± 0.32, is about one-fifth of the Archimedean spiral, 2.77 ± 1.60.

Compared with the reference data set in Fig. 6a, which was acquired with a noninterleaved Archimedean spiral pattern, phantom images were degraded by eddy current effects when data acquisition was performed with the interleaved Archimedean pattern of type A: Fig. 6b. The image quality was completely restored in case of the interleaved spiral phyllotaxis pattern in Fig. 6c. The in vivo experiments not only confirmed that eddy currents are strongly reduced with the interleaved spiral phyllotaxis pattern but also residual streaking artifacts were significantly reduced. This trend was also reflected by SNR and CNR measurements. Compared with the reference data, both SNR and CNR of images acquired with the interleaved Archimedean pattern decreased from an average of 5.71 ± 1.41 to 4.17 ± 1.05 and from 2.46 ± 0.94 to 1.81 ± 0.83, respectively. With the spiral phyllotaxis pattern, SNR and CNR of 6.42 ± 1.71 and 2.96 ± 1.16 were even superior to the reference. The vessel sharpness of 0.74 ± 0.13 in case of the spiral phyllotaxis pattern was slightly superior to both the interleaved and even the noninterleaved Archimedean spiral pattern with values of 0.64 ± 0.14 and 0.68 ± 0.12, respectively. Irrespectively of the overall image quality and of the trajectory used for acquisition, residual fat signal around the coronary vessels could be detected in different locations in all the image data.

DISCUSSION

The current implementation of the 3D radial trajectory based on the spiral phyllotaxis pattern features an overall uniformity in the distribution of the readouts. In fact, although the RSD of the spiral phyllotaxis is higher than that of the uniform Archimedean spiral, a density compensation algorithm for uniform distribution is considered to be sufficient when the RSD is less than 10% (22). Furthermore, the new trajectory intrinsically provides an arrangement of the readouts that minimizes eddy current effects, if interleaved with a Fibonacci number. Nevertheless, an

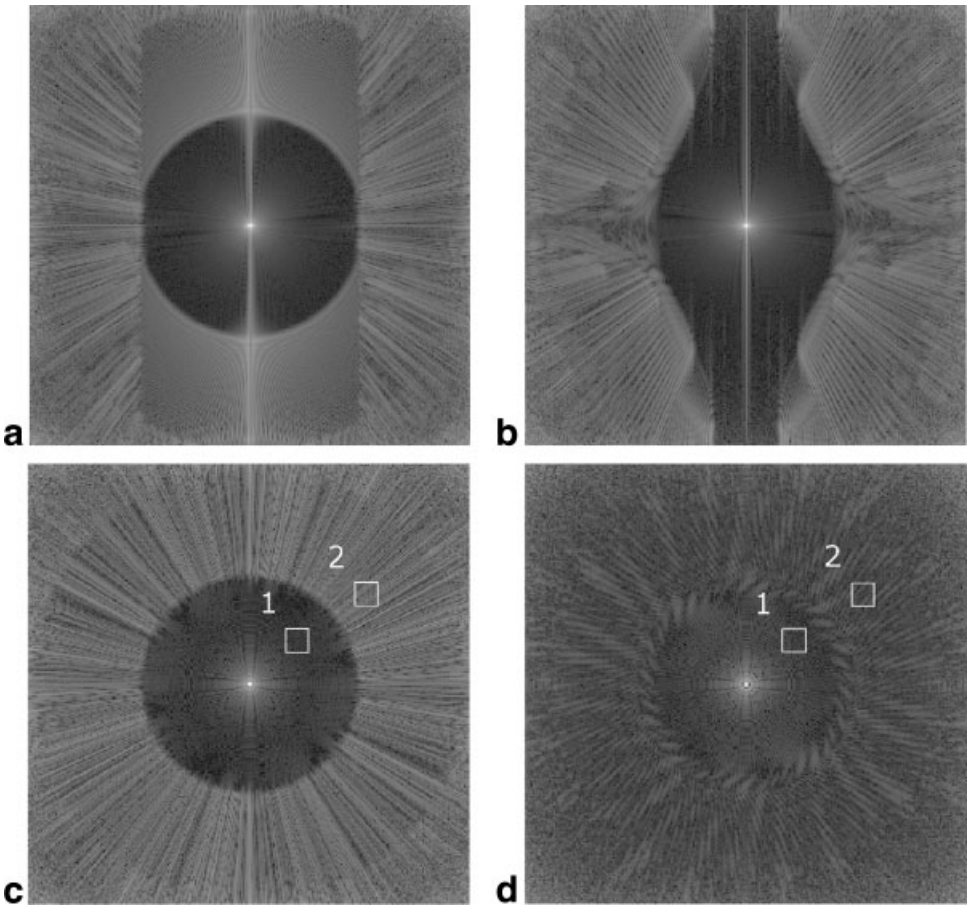

FIG. 5. Comparison between the PSFs of the 3D radial trajectories based on the uniform Archimedean spiral pattern (**a**,**c**) and on the new spiral phyllotaxis pattern (**b**,**d**) over two FOVs, both with an undersampling ratio of 22% and total number of readouts $N = 12{,}818$. The plots represent the central coronal (a,b) and the central transversal (c,d) slices of a 3D volume with the signal intensities plotted on a logarithmic scale. Whereas the amplitude of the central peak is the same for both PSFs, the overall signal distribution of the streaking patterns differs significantly.

effective sorting of the readouts is also feasible when a non-Fibonacci number of interleaves is selected. Alternative mathematical models for constructing the spiral phyllotaxis can be implemented to further increase the packing efficiency of the trajectory. These can include the introduction of a variable offset to the azimuthal shift in Vogel's formula (4) or the addition of other constraints, e.g., the target distance between adjacent readouts (5). In these cases, the consistency of the intrinsic arrangement of the readouts needs to be verified and a trade-off between feasible improvements and computational effort has to be considered.

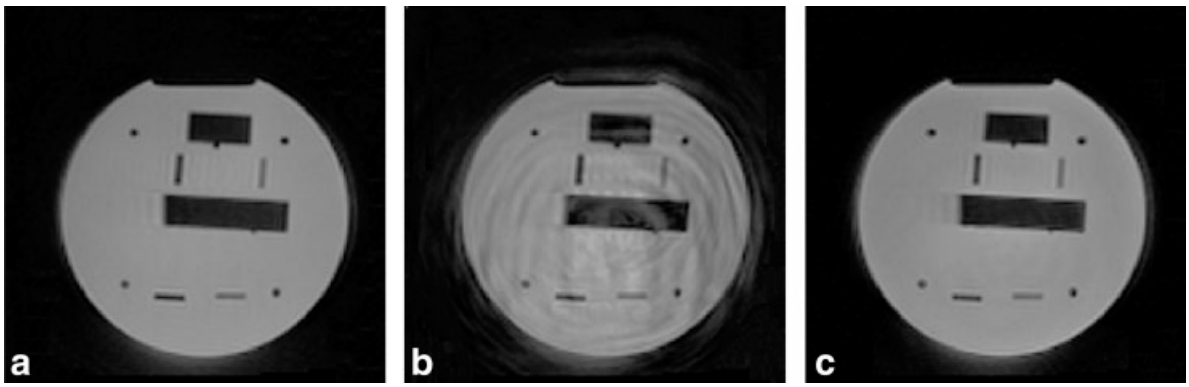

FIG. 6. Phantom experiments with an SSFP sequence demonstrating the sensitivity of different types of 3D radial sampling patterns to eddy currents. Since the overall distribution of readouts was uniform independently on the sampling pattern, the same image reconstruction program including the density compensation function was used in all cases. (**a**) Reference image acquired with a non-interleaved Archimedean spiral pattern (12,818 readouts): only minor ringing artifacts are visible. (**b**) Image acquired with the Archimedean spiral pattern interleaved with the straightforward approach of type A (12,818 readouts in 377 interleaves and 34 readouts per interleave): the image quality is degraded by severe eddy current effects. (**c**) Novel interleaved 3D spiral phyllotaxis pattern (12,818 readouts in 377 interleaves and 34 readouts per interleave): the image quality was completely restored.

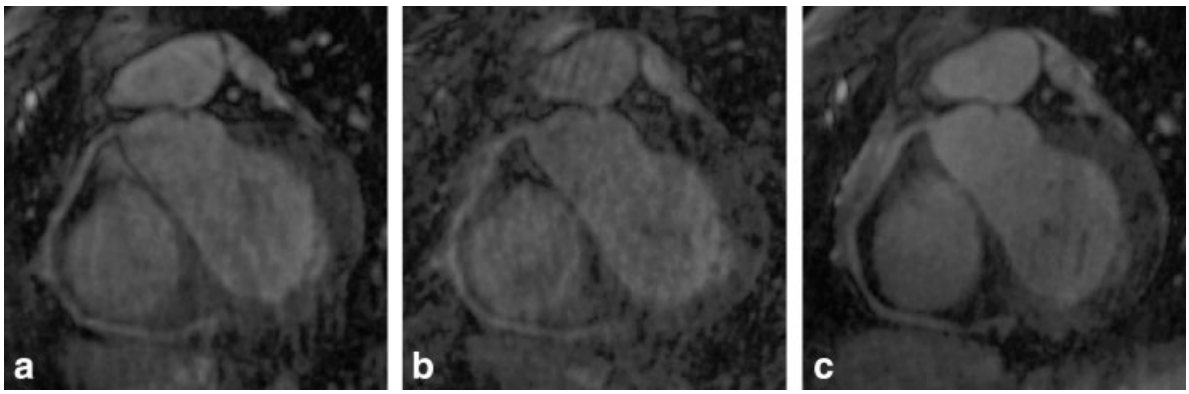

FIG. 7. Reformatted images of the RCA are depicted for acquisitions obtained with the three different 3D radial trajectories reconstructed with a gridding algorithm featuring identical density compensation settings. (**a**) Reference images, which were acquired with a noninterleaved 3D Archimedean spiral pattern, were compared with (**b**) images from Archimedean spiral pattern acquired with the straightforward interleaving approach of type A. In the latter case, the image quality was degraded by eddy current effects. In images that were acquired with the novel interleaved 3D spiral phyllotaxis pattern (**c**), the overall image quality was even improved with respect to the reference. The new trajectory features superior interleaving properties while preserving an overall uniform sampling distribution.

Phantom experiments showed that the final image quality obtained with the interleaved spiral phyllotaxis pattern is close to the uniform Archimedean noninterleaved spiral pattern. Although eddy current effects were avoided, a slight residual degradation of the image quality might be explained by a disadvantage of the novel trajectory when the FOV is larger than the imaged object. The reason for the significant reduction of streaking in vivo can be found in the substantial difference in the PSFs of the trajectories used. Since RF excitation was nonselective and the object exceeded the FOV in SI direction by far, the novel trajectory can be expected to be more robust against aliasing artifacts in this direction. The difference in the transversal orientation of the PSFs might also have a positive effect, if aliasing energy of anterior-posterior or left-right structures, such as the chest wall or the arms, is taken into account. In general, the novel trajectory intrinsically avoids non-uniform distribution of the signal in k-space caused by transient signal over the acquisition time of one interleave. This, in fact, might also positively affect the overall image quality reflected in the results of SNR and CNR. Nevertheless, considering the number of cases analysed, neither the superior SNR and CNR, nor the improvement in vessel sharpness can be rated as statistically significant. In the latter case, the improvement is more likely to be caused by the general improvement of the image quality, rather than a difference in the PSFs, since the innermost part of the two PSFs is practically identical.

The image quality of all in vivo data sets was affected by the prolonged acquisition times, usually caused by irregularities in the breathing pattern of the volunteers and/or by a sub-optimal placement of the beam navigator. For this reason, coronary MRI implementing respiratory self-navigation methods is highly desired. An extra readout constantly oriented along the SI direction can be added at the beginning of each interleave of the spiral phyllotaxis pattern and used for the detection of the respiratory motion (22). If the extra readout is not taken into account in the reconstruction, then all the properties of the trajectory remain unchanged. Therefore, the 3D spiral phyllotaxis pattern is intrinsically prepared for self-navigation.

The spiral phyllotaxis pattern also holds further mathematical properties that can be exploited for clinical applications. In the highly interleaved setup required for coronary MRI, this trajectory automatically arranges in such a way that each new interleave is placed in the largest azimuthal gap left by the preceding set of interleaves and always divides the gap according to the golden ratio, thus providing an almost uniform sampling pattern over time (9). As a consequence, subsets of successive interleaves at arbitrary time points can be used to reconstruct sub-sampled imaging volumes with high spatial uniformity. In this context of temporal stability, an experimental comparison between the new 3D spiral phyllotaxis pattern and the adaptive radial 3D projection reconstruction method, recently proposed in (8) and based on multi-dimensional golden means, is considered very interesting. Moreover, Fig. 2a.2 and 2c.2 suggest that the distribution of the readouts in the single interleave in a highly interleaved setup is more uniform for the spiral phyllotaxis than for the uniform Archimedean spiral, when a non-Fibonacci number of interleaves is selected. The overall sampling uniformity of the spiral phyllotaxis makes it attractive for applications dealing with highly undersampled data. In this context, the impact of parallel imaging techniques for non-Cartesian trajectories, such as (29) can be explored.

Furthermore, the integration of methods exploiting the redundancy of the information contained in the images, such as HYPR (30) or iterative reconstruction methods like compressed sensing (31), to the 3D spiral phyllotaxis pattern represents an attractive possibility (32). Such combinations, in fact, could lead not only to highly reduced total examination times for applications such as coronary MRI but also to feasible applications in dynamic studies, e.g., cine or perfusion MRI. Eventually, concerning the sub-optimal effectiveness of the fat saturation pulses, better results could be achieved by improving the shimming procedure within the imaged volume. On the other hand, since

the fat saturation pulse is applied only once at the beginning of each interleave, further advantages could derive from the acquisition of a smaller number of readouts per interleave.

SUMMARY AND OUTLOOK

The new 3D radial trajectory based on the spiral phyllotaxis pattern is a "natural" solution for radial 3D MRI. This trajectory features a simple mathematical implementation and can be easily integrated into existing 3D radial acquisition frameworks without the need for a dedicated density compensation algorithm. The spiral phyllotaxis pattern combines both an overall uniformity of the distribution of the readouts and an intrinsic arrangement of the readouts that reduces eddy current effects, thus overcoming the limitations of the reference approaches. This work, and in particular the good results obtained in the in vivo experiments, demonstrated that the radial 3D trajectory based on the spiral phyllotaxis pattern is a robust solution for volumetric acquisitions where both radial undersampling and motion are involved and where a high interleaving setup is required. The application of the new trajectory for self-navigation and the integration of motion correction algorithms will be subject to future investigations.

REFERENCES

1. Douady S, Couder Y. Phyllotaxis as a dynamical self organizing process part I: the spiral modes resulting from time-periodic iterations. J Theor Biol 1996;178:255–274.
2. Mathai AM, Davis TA. Constructing the sunflower head. Math Biosci 1974;20:117–133.
3. Vogel H. A better way to construct the sunflower head. Math Biosci 1979;44:179–189.
4. Ridley JN. Computer simulation of contact pressure in capitula. J Theor Biol 1982;95:1–11.
5. Fowler DR, Prusinkiewicz P, Battjes J. A collision-based model of spiral phyllotaxis. SIGGRAPH Comp Graph 1992;26:361–368.
6. Li CR, Ji AL, Gao L, Cao ZX. Stressed triangular tessellations and fibonacci parastichous spirals on Ag Core/SiO_2 shell microstructures. Adv Mater 2009;21:4652–4657.
7. Cline HE, Anthony TR. Uniform k-space sampling with an interleaved Fibonacci spiral acquisition. Proceedings of the 7th Annual Meeting of ISMRM, Philadelphia, USA, 1999. p. 1657.
8. Chan RW, Ramsay EA, Cunningham CH, Plewes DB. Temporal stability of adaptive 3D radial MRI using multidimensional golden means. Magn Reson Med 2009;61:354–363.
9. Winkelmann S, Schäffter T, Köhler T, Eggers H, Dössel O. An optimal radial profile order based on the golden ration for time resolved MRI. IEEE Trans Med Imaging 2007;26:68–76.
10. Lu W, Hargreaves BA. Multiresolution field map estimation using golden section search for water-fat separation. Magn Reson Med 2008;60:236–244.
11. Börnert P, Jensen D. Coronary artery imaging at 0.5 T using segmented 3D echo planar imaging. Magn Reson Med 1995;34:524–531.
12. Stuber M, Botnar RM, Danias PG, Sodickson DK, Kissinger KV, Van Cauteren M, De Becker J, Manning WJ. Double-oblique free-breathing high resolution three-dimensional coronary magnetic resonance angiography. J Am Coll Cardiol 1999;34:524–531.
13. Lauzon ML, Rutt BK. Effects of polar sampling in k-space. Magn Reson Med 1996;36:940–949.
14. Barger AV, Block VF, Toropov Y, Grist TM, Mistretta CA. Time-resolved contrast-enhanced imaging with isotropic resolution and broad coverage using an undersampled 3D projection trajectory. Magn Reson Med 2002;48:297–305.
15. Shu Y, Riederer SJ, Bernstein MA. Three-dimensional MRI with and undersampled spherical shells trajectory. Magn Reson Med 2006;56:553–562.
16. Stehning C, Börnet P, Nehrke K, Eggers H, Dössel O. Fast isotropic volumetric coronary MR angiography using free-breathing 3D radial balanced FFE acquisition. Magn Reson Med 2004;52:197–203.
17. Pipe JG, Menon P. Sampling density compensation in MRI: rationale and an iterative numerical solution. Magn Reson Med 1999;41:179–186.
18. Hoge RD, Kwan RKS, Pike GB. Density compensation functions for spiral MRI. Magn Reson Med 1997;38:117–128.
19. Kim WY, Stuber M, Kissinger KV, Andersen NT, Manning WJ, Botnar RM. Impact of bulk cardiac motion on right coronary MR angiography and vessel wall imaging. J Magn Reson Imaging 2001;14:383–390.
20. McLeish K, Hill LGD, Atkinson D, Blackall JM, Razavi R. A study of the motion and deformation of the heart due to respiration. IEEE Trans Med Imaging 2002;21:1142–1150.
21. Wang Y, Riederer SJ, Ehman RL. Respiratory motion of the heart: kinematics and the implications for the spatial resolution in coronary imaging. Magn Reson Med 1995;33:713–719.
22. Stehning C, Börnet P, Nehrke K, Eggers H, Stuber M. Free-breathing whole-heart coronary MRA with 3D radial SSFP and self-navigated image reconstruction. Magn Reson Med 2005;54:476–480.
23. Scheffler K, Henning J. Eddy current optimized phase encoding schemes to reduce artifacts in balanced SSFP imaging. Proceedings of the 11th Annual Meeting of ISMRM, Toronto, Canada, 2003. p. 294.
24. Wong STS, Roos MS. A strategy for sampling on a sphere applied to 3D selective RF pulse design. Magn Reson Med 1994;32:778–784.
25. Nielles-Vallespin S, Spier P, Bi X, Li D, Müller E. Navigator-gated whole heart coronary MRI: comparison of 3D TrueFisp Cartesian and radial acquisitions. Proceedings of the 14th Annual Meeting of ISMRM, Seattle, Washington, USA, 2006. p. 366.
26. Piccini D, Littmann A, Schmitt P, Zenge MO. Spiral phyllotaxis: a better way to construct a 3D radial trajectory in MRI. Proceedings of the 18th Annual Meeting of ISMRM, Stockholm, Sweden, 2010. p. 4972.
27. Nielles-Vallespin S, Weber MA, Bock M, Bongers A, Speier P, Combs SE, Wöhrle J, Lehmann-Horn F, Essig M, Shad LR. 3D radial projection technique with ultrashort echo times for sodium MRI: clinical applications in human brain and skeletal muscle. Magn Reson Med 2007;57:74–81.
28. Li D, Carr JC, Shea SM, Zheng J, Deshpande VS, Wielopolski PA, Finn JP. Coronary arteries: magnetization-prepared contrast-enhanced three-dimensional volume-targeted breath-hold MR angiography. Radiology 2001;219:270–277.
29. Seiberlich N, Breuer FA, Blaimer M, Barkauskas K. Non-cartesian data reconstruction using GRAPPA operator gridding (GROG). Magn Reson Med 2007;58:1257–1265.
30. Mistretta CA, Wieben O, Velikina J, Block W, Perry J, Wu Y, Johnson K, Wu Y. Highly constrained backprojection for time-resolved MRI. Magn Reson Med 2006;55:30–40.
31. Lustig M, Donoho D, Pauly JM. Sparse MRI: the application of compressed sensing for rapid MRI imaging. Magn Reson Med 2007;58:1182–1195.
32. Doneva M, Eggers H, Rahmer J, Börnert P, Mertins A. Highly undersampled 3D golden ratio radial imaging with iterative reconstruction. Proceedings of the 16th Annual Meeting of ISMRM, Toronto, Canada, 2008. p. 336.